

Mapping Apparent Eccentricity and Residual Ensemble Anisotropy in the Gray Matter Using Angular Double-Pulsed-Field-Gradient MRI

Noam Shemesh,¹ Daniel Barazany,² Ofer Sadan,³ Leah Bar,⁴ Yuval Zur,⁵ Yael Barhum,^{6,7} Nir Sochen,⁴ Daniel Offen,^{6,7} Yaniv Assaf,² and Yoram Cohen^{1*}

Conventional diffusion MRI methods are mostly capable of portraying microarchitectural elements such as fiber orientation in white matter from detection of diffusion anisotropy, which arises from the coherent organization of anisotropic compartments. Double-pulsed-field-gradient MR methods provide a means for obtaining microstructural information such as compartment shape and microscopic anisotropies even in scenarios where macroscopic organization is absent. Here, we apply angular double-pulsed-gradient-spin-echo MRI in the rat brain both *ex vivo* and *in vivo* for the first time. Robust angular dependencies are detected in the brain at long mixing time (t_m). In many pixels, the oscillations seem to originate from residual directors in randomly oriented media, i.e., from residual ensemble anisotropy, as corroborated by quantitative simulations. We then developed an analysis scheme that enables one to map of structural indices such as apparent eccentricity (aE) and residual phase (φ) that enables characterization of the rat brain in general, and especially the rat gray matter. We conclude that double-pulsed-gradient-spin-echo MRI may in principle become important in characterizing gray matter morphological features and pathologies in both basic and applied neurosciences. Magn Reson Med 68:794–806, 2012. © 2011 Wiley Periodicals, Inc.

Key words: diffusion MRI; rat brain; double-PFG MRI; anisotropy; gray matter

Central-nervous-system (CNS) tissues are characterized by intricate microarchitectural features which, through their organization and networking, give rise to the highly complex functions of the CNS (1). One of the most useful contrast mechanisms for studying CNS microarchitecture

is based on the sensitization of the MRI signal to diffusion of endogenous water molecules because the diffusion process is highly affected by restricting boundaries. Indeed, in the early days of diffusion-weighted imaging, it was demonstrated that early ischemia can be detected (2) and that water diffusion appears anisotropic at least in white matter (WM) (3). Currently, diffusion-tensor-imaging (DTI) (4) is widely used to study, *inter alia*, structural connectivity and tractography of normal (5,6), developmental (7) and pathological (8) WM tissues. Recently, diffusion MR was even used to study functional (9,10) aspects of the CNS. In all these DTI applications, the diffusion anisotropy that is detected is in fact ensemble anisotropy (eA), arising from coherent organization of anisotropic compartments. In regions that are much less ordered, such as mature gray matter, conventional diffusion MRI methods exhibit low anisotropy (11–13), and thus relatively low contrast is obtained.

The double-pulsed-field-gradient (d-PFG) MR methodology (14–18) is an extension of conventional diffusion MR, applying two pairs of diffusion-sensitizing PFGs that are separated by a mixing time (t_m). Figure 1a shows an imaging sequence based on a double-pulsed-gradient-spin-echo (d-PGSE) sequence. One unique variant of d-PFG MR, namely the angular d-PFG MR methodology was first theoretically proposed by Mitra in 1995 (19). The angular experiment is performed by fixing the mixing time, diffusion periods, and gradient durations and amplitudes, and only varying the angle ψ between the gradients (Fig. 1b). The initial theory (19) predicted that at low q -values, a bell-shaped signal intensity as function of ψ ($E(\psi)$) would emerge at short t_m , but strictly for restricted diffusion (as opposed to free, gaussian or multi-gaussian diffusion processes). These bell-shaped $E(\psi)$ dependencies were predicted to be proportional to the restricting length scale; therefore, angular d-PFG MR could potentially offer information on compartment size without requiring very strong gradients. Indeed, such bell-shaped $E(\psi)$ dependencies were only very recently observed experimentally for the first time in MRI (20,21) as well as in d-PFG NMR spectroscopy in controlled organized systems (22–24).

Further recent progress in the theory and simulations of angular d-PFG MR suggested that it could uniquely report on microstructure even when there is no macroscopic ordering within the specimen (25–28), i.e., in systems where conventional diffusion MR yield little microstructural information owing to the low ensemble

¹School of Chemistry, The Raymond and Beverly Sackler Faculty of Exact Sciences, Tel Aviv University, Tel Aviv, Israel.

²Department of Neurobiology, The George S. Wise Faculty of Life Sciences, Tel Aviv University, Tel Aviv, Israel.

³Department of Neurology, Tel-Aviv Medical Center, Tel Aviv, Israel.

⁴School of Mathematical Sciences, The Raymond and Beverly Sackler Faculty of Exact Sciences, Tel Aviv University, Tel Aviv, Israel.

⁵GE Healthcare, Haifa, Israel.

⁶Human Molecular Genetics and Biochemistry Department, Sackler Faculty of Medicine, Tel Aviv University, Tel Aviv, Israel.

⁷Felsenstein Medical Research Center, Rabin Medical Center, Petah Tikva, Israel.

Grant sponsors: CONNECT consortium administered by the European Commission under framework package 7, Israel Science Foundation, The Raymond and Beverly Sackler Center for Biophysics, Tel Aviv University.

*Correspondence to: Yoram Cohen, Ph.D., The Sackler Faculty of Exact Sciences, School of Chemistry, Tel Aviv University, Ramat Aviv, Tel Aviv 69978, Israel. E-mail: ycohen@post.tau.ac.il

Received 6 May 2011; revised 5 October 2011; accepted 24 October 2011. DOI 10.1002/mrm.23300

Published online 29 November 2011 in Wiley Online Library (wileyonlinelibrary.com).

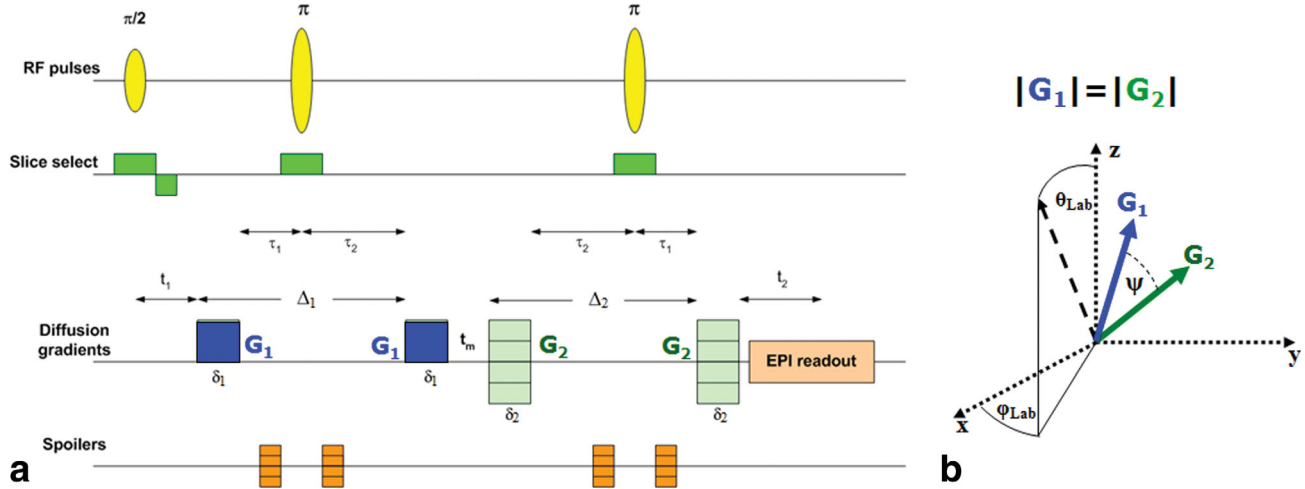


FIG. 1. **a:** The d-PGSE MRI sequence with EPI readout used in this study. **b:** The angular d-PFG experiment is performed by keeping the gradient amplitudes constant, while varying the angle ψ between these two gradient vectors. The azimuthal and polar angles in the lab frame, ϕ_{Lab} and θ_{Lab} , are also defined. Experiments were performed in the X-Y plane, ie, with \mathbf{G}_1 pointing along the x-direction and the orientation of \mathbf{G}_2 was varied in the X-Y plane. Under these definitions, the rats were aligned with their anterior-posterior axis pointing towards the x-axis; note that under these definitions, this axis in fact coincides with the direction of \mathbf{B}_0 . [Color figure can be viewed in the online issue, which is available at wileyonlinelibrary.com.]

anisotropy present. At long t_m , the $E(\psi)$ plots of angular d-PFG MR were predicted to bear signatures for compartment shape anisotropy, thus offering a unique possibility to distinguish between compartments having different eccentricities (26). Indeed, modulated $E(\psi)$ curves at long t_m were recently observed for the first time in well-controlled systems (29) as well as in various heterogeneous chemical and biological systems (30) and very recently, randomly oriented anisotropic compartments in isolated pig gray matter were detected for the first time (31). Additionally, ψ -independent $E(\psi)$ plots were detected for spherical yeast cells (30). In all the earlier cases, conventional diffusion MR methods only showed isotropic diffusion, thus demonstrating that unique microstructural information could be obtained from angular d-PFG MR. Previous studies also used d-PFG MR experiments at only two directions to infer on eccentricities in elongated yeast cells (15) and liquid crystals (16) or to infer on the presence of underlying heterogeneity in the spinal cord (18).

Tensor approaches to angular d-PFG MR have been recently emerging that provide indices of microscopic anisotropy that are invariant to rotation (32,33) as well as the relationship of the signal decay with the displacement correlation tensor (34). Approaches aimed at increasing the extent of the angular dependencies by applying multiple concatenations have also been theoretically suggested recently (35,36) and a “phase-gymnastics” approach has been presented to more intuitively explain the signal differences at $\psi = 0^\circ$ and 180° (37). Recently, Özarslan’s theoretical findings (25–27) were reproduced by extending the matrix formalism approach to angular d-PFG MR (38). Subsequently, an experimental study on a pig spinal cord phantom showed that d-PFG MRI experiments (dubbed double-wave-vector experiments) could be performed on a clinical scanner (39).

Here, we perform angular d-PFG MRI at long mixing time (t_m) for the first time on a rat brain both ex vivo and in vivo. We demonstrate that different modulated

$E(\psi)$ plots exist in different regions of the brain, including in the gray matter. We show that in some regions, the $E(\psi)$ plots are modulated by nonzero phase. Quantitative simulations show that these phases can be attributed to residual ensemble anisotropy in otherwise mostly randomly oriented compartments. A phenomenological quantitative approach for characterizing indices such as apparent eccentricity (aE) and residual phase (ϕ) is given, and maps based on these parameters are shown to offer new sources of contrast, especially within the gray matter. Finally, we show that similar findings can be obtained in vivo in the rat brain using a conventional animal MRI scanner.

MATERIALS AND METHODS

All animal experiments were approved by the University Committee of Animal Use for Research and Education. Male Wistar rats ($N = 5$) weighing ~ 300 g were intracardially perfused with 4% paraformaldehyde, and their brains were removed into a 4% paraformaldehyde solution. The ex vivo rat brains were immersed in phosphate-buffered saline (PBS) overnight before the MRI experiments. The brains were placed in a 15-mm glass tube filled with Fluorinert. A septum was used to seal the tube and Fluorinert was injected through the septum until no air bubbles were observed in the tube.

All MRI experiments were performed on a Bruker Biospec 7-T scanner (Bruker Biospin, Karlsruhe, Germany), equipped with a gradient system capable of producing up to 400 mT/m. The tube containing the brain was inserted such that the anterior–posterior axis of the brain was aligned along the direction of the main magnetic field. The orientation of the brain was carefully adjusted in the magnet such that an imaginary line connecting the dorsal edges of the two hemispheres was horizontal. A volume coil was used for transmitting, whereas a quadrature coil placed directly above the tube was used as the receiving coil.

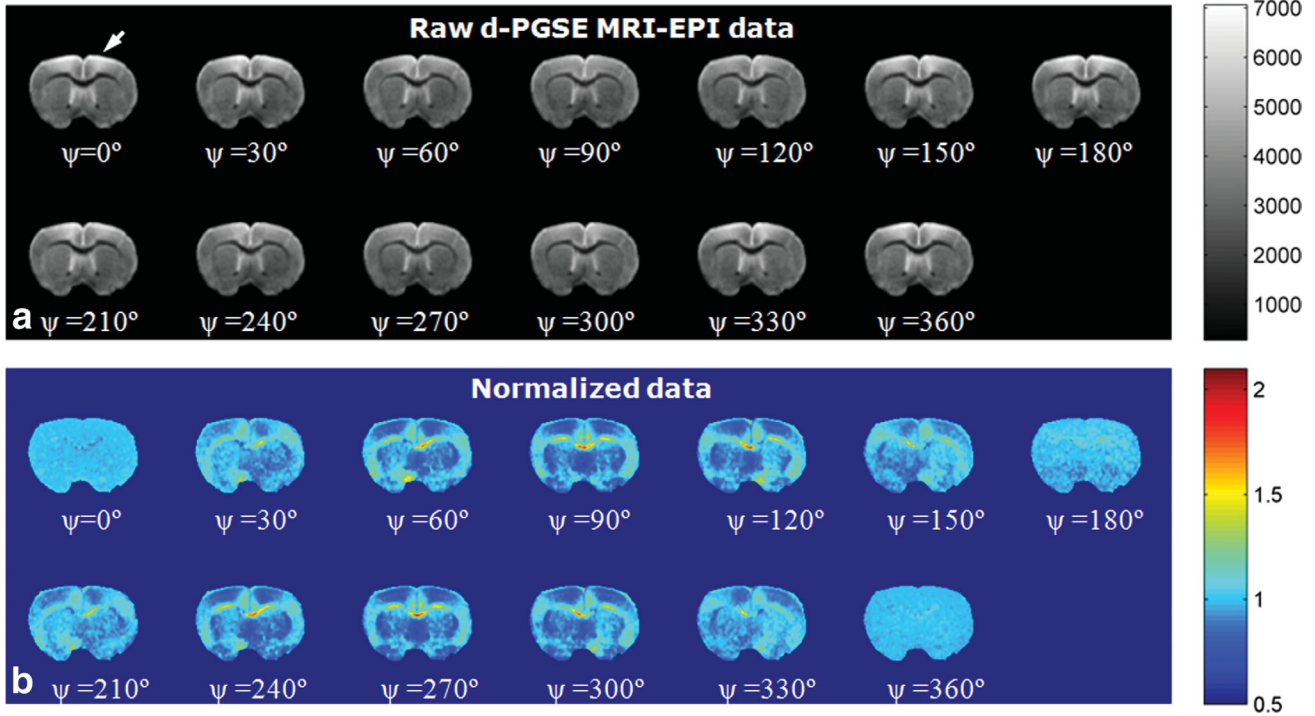


FIG. 2. **a**: The raw $E(\psi)$ data from an angular d-PGSE MRI experiment with EPI readout on an ex vivo rat brain that was conducted in the X - Y plane (Fig. 1). Note the oscillatory signal intensity variance along the different ψ angles. The arrow indicates on areas in the cortex for which the oscillations are visually clear. **b**: $E(\psi)_{\text{norm}}$ images for the 13 ψ values. After normalizing the data, the oscillations are not influenced by the initial value of $E(\psi = 0^\circ)$ in every voxel, and any bias effects are removed. The oscillations are now purely relative to the $\psi = 0^\circ$ image, and their magnitude represents structural parameters as explained in the text. [Color figure can be viewed in the online issue, which is available at wileyonlinelibrary.com.]

In the in vivo measurement, anesthesia was induced using 4% isoflurane (Vetmarket LTD., Petah Tikva, Israel) carried by a flow of 95% O_2 , which was gradually reduced to $\sim 1.5\%$ isoflurane. The rat was placed on a heated bed, and its respiration rate was monitored. The same transmit/receive coils were used as for the ex vivo setup.

A d-PGSE MRI sequence with echo-planar imaging (EPI) readout was written in-house, allowing for completely free control of the variables \mathbf{q}_1 , \mathbf{q}_2 , Δ_1 , Δ_2 , δ_1 , δ_2 , and t_m . In all experiments in this study, we chose $|\mathbf{q}_1| = |\mathbf{q}_2|$, $\delta_1 = \delta_2$, and $\Delta_1 = \Delta_2$. The angular d-PGSE MRI experiments were performed in a similar fashion to the previously described d-PFG spectroscopy experiments (40). For a review on the d-PFG MR methodology in general and on angular d-PFG MR in particular, see Ref. 41. Briefly, $\Delta_1 = \Delta_2$, $\delta_1 = \delta_2$, and the q -value were fixed. \mathbf{G}_1 was set in the x -direction, and the orientation of \mathbf{G}_2 was varied in the X - Y plane along 13 ψ -values between 0° and 360° . The rat was aligned with its anterior-posterior axis pointing toward the x -direction (defined in Fig. 1b). The X - Y plane is therefore defined as the axial plane (the plane perpendicular to the slice as shown in Fig. 2 and parallel to the slice as shown in Fig. 6d-f).

Image Analysis

A code was written in Matlab® to analyze the images. The analysis included five steps. First, the 13 $E(\psi)$ images were realigned and smoothed using a small gaussian kernel of twice the voxel size. Second, a reference image was created according to $E_{\text{ref}} = \{E(\psi = 0^\circ) + E(\psi = 360^\circ)\}/2$ and each $E(\psi)$ image was normalized to this reference image, i.e., $E(\psi)_{\text{norm}} = E(\psi)/E_{\text{ref}}$. Third, a mask was manually marked for the brain. Fourth, a Levenberg-Marquardt non-linear-least-squared routine was used to fit the data to the following equation:

$$E(\psi)_{\text{norm}} = 1 - aE \cdot [\sin^2(\psi + \varphi)] + C \quad [1]$$

where aE , φ , and C are fitted parameters. The analysis was performed pixel-by-pixel. In the fifth and final steps, maps of the fitted parameters were generated. For the parameter φ , a symmetrized color-coded map was additionally created by assigning equal colors to the same positive and negative values of φ . In some cases, the absolute value of aE , $|aE|$ was mapped. Note that in these analyses, a diffusion coefficient is not assumed because Eq. 1 provides a phenomenological description of the oscillating data. We also note that a rather similar expression for the actual signal decay in d-PFG MR for a single cylinder was obtained analytically in Ref. 25.

DTI images were analyzed by extracting the diffusion tensor using the DiVa tool (<http://diva-dti.sourceforge.net/>) in Matlab®. The same mask was applied for d-PGSE MRI and DTI images. The eigenvalues, eigenvectors, FA, and color-coded FA maps were generated from the DTI data.

Experimental Parameters for the MRI Experiments

For the brains shown in Figs. 5 and 7 (each coming from a different rat), the following parameters were used: $t_m =$

15 ms, $\delta_1 = \delta_2 = 3.5$ ms, $\Delta_1 = \Delta_2 = 20$ ms, $|G_1| = |G_2| = 336$ mT/m, resulting in a $2q$ value of 1000 cm^{-1} . The field of view (FOV) was $1.96 \times 1.96 \text{ cm}^2$ and the slice thickness was $800 \text{ }\mu\text{m}$. A matrix of 156×156 was chosen, resulting in an in-plane resolution of $125 \times 125 \text{ }\mu\text{m}^2$. The repetition time/echo time (TR/TE) of the d-PGSE MRI experiments was 2800/65 ms (TE refers to the entire duration from the first radiofrequency pulse to the time of acquisition). The number of averages was 160, resulting in ~ 6.5 h of scan time per dataset.

For the brain shown in Fig. 6a–c, the following parameters were used: $t_m = 15$ ms, $\delta_1 = \delta_2 = 3.8$ ms, $\Delta_1 = \Delta_2 = 25$ ms, and $|G_1| = |G_2| = 340$ mT/m, resulting in a $2q$ value of 1100 cm^{-1} . The FOV was $1.8 \times 1.8 \text{ cm}^2$ and the slice thickness was $800 \text{ }\mu\text{m}$. A matrix of 128×128 was chosen, resulting in an in-plane resolution of $140 \times 140 \text{ }\mu\text{m}^2$. The TR/TE was 2800/82 ms. The number of averages was 320, resulting in ~ 13 h scan time. For the brain shown in Fig. 6d–f, the same parameters as for the brain of Fig. 6a–c were used except the orientation was axial, the FOV was $2.28 \times 2.28 \text{ cm}^2$, and the matrix size was 182×182 resulting in the same in-plane resolution of $125 \times 125 \text{ }\mu\text{m}^2$.

For the brain shown in Fig. 8, the following parameters were used: $t_m = 15$ ms, $\delta_1 = \delta_2 = 3.5$ ms, $\Delta_1 = \Delta_2 = 20$ ms, and $|G_1| = |G_2| = 336$ mT/m, resulting in a $2q$ value of 1000 cm^{-1} . The FOV was $1.96 \times 1.96 \text{ cm}^2$ and the slice thickness was $800 \text{ }\mu\text{m}$. A matrix of 156×156 was chosen, resulting in an in-plane resolution of $125 \times 125 \text{ }\mu\text{m}^2$. The TR/TE was 2800/68 ms. For the DTI scans, a SE-DTI sequence with EPI readout was used with diffusion parameters that were set to be comparable to those outlined for d-PGSE MRI earlier, i.e., for DTI, Δ was set to be equal to Δ_1 and δ was set to be equal to δ_1 above. DTI was performed in 15 directions with $|G| = 246$ mT/m corresponding to a b -value of 1000 s/mm^2 . The in-plane resolution and slice thickness were exactly as for the d-PGSE MRI sequence.

For the in vivo rat brain (Fig. 9), a relatively anterior slice was chosen because it contains much gray matter. The following parameters were used: $t_m = 15$ ms, $\delta_1 = \delta_2 = 3$ ms, $\Delta_1 = \Delta_2 = 17$ ms, and $|G_1| = |G_2| = 360$ mT/m, resulting in a $2q$ value of 920 cm^{-1} . The FOV was $2.28 \times 2.28 \text{ cm}^2$ and the slice thickness was $800 \text{ }\mu\text{m}$. A matrix of 162×162 was chosen, resulting in an in-plane resolution of $140 \times 140 \text{ }\mu\text{m}^2$. The TR/TE was 2000/62 ms. The number of averages was 72, resulting in ~ 2 h of scan time. A SE-DTI sequence with EPI readout was used with diffusion parameters that were set to be comparable to those outlined for d-PGSE MRI earlier, i.e., for DTI, Δ was set to be equal to Δ_1 and δ was set to be equal to δ_1 . DTI was performed in 30 directions at a b -value of 1000 s/mm^2 . The in-plane resolution and slice thickness were exactly as for the d-PGSE MRI sequence. Note that the TEs described earlier for all methods refer to the central k -space line.

For histology, the brains were transferred to a solution of 30% sucrose in PBS for 48 h at 4°C and transferred to PBS. The brains were then cryosectioned to $\sim 10\text{-}\mu\text{m}$ -thick slices. Sections were incubated in a blocking and permeabilization solution (5% normal goat serum, 1% bovine serum albumin, and 0.5% Triton X-100 in PBS) and incubated with a primary antibody, mouse anti tyro-

sine-hydroxylase (TH), diluted 1:100 (Sigma-Aldrich) overnight at 4°C . After washing with PBS, sections were incubated with a biotinylated secondary antibody (goat anti-mouse, Invitrogen, Carlsbad, CA, 1:200) for 1 h followed by 488-alexa conjugated streptavidin (1:500, Invitrogen).

Simulations

The general theory for diffusion-induced signal decay in d-PFG MR, first published in Refs. 26 and 27 was implemented in Matlab®. For the simulations in this study, the $E(\psi)$ signal was computed using the expanded analytical solutions given in the earlier references. $E(\psi)_{\text{norm}}$ plots were obtained by dividing $E(\psi)$ with $E(\psi = 0^\circ)$. The following parameters were used for all simulations: In all cases, capped cylindrical compartments were considered, having a radius, $r_0 = 4 \text{ }\mu\text{m}$ and length, $L = 20 \text{ }\mu\text{m}$. The following d-PFG parameters were used: $t_m = 50$ ms, $\delta_1 = \delta_2 = 1.5$ ms, $\Delta_1 = \Delta_2 = 20$ ms, and $|G_1| = |G_2| = 782$ mT/m, resulting in a $2q$ value of 1000 cm^{-1} . G_1 was set in the x -direction ($\varphi_{\text{Lab}} = 0^\circ$) and $\theta_{\text{Lab}} = 90^\circ$, where φ_{Lab} and θ_{Lab} are the azimuthal angle and polar angle in lab coordinates, respectively (see Fig. 1b), and the angle ψ was varied in the X - Y plane. The simulation considered the following three cases. (1) Cylinders were completely randomly oriented along both φ_{Lab} and θ_{Lab} . (2) A residual coherent alignment was allowed for 30% of the cylinders along $\varphi_{\text{Lab}} = 45^\circ$, $\theta_{\text{Lab}} = 90^\circ$, whereas the rest of the cylinders were randomly oriented along both φ_{Lab} and θ_{Lab} . (3) A residual coherent alignment was allowed for 30% of the cylinders along $\varphi_{\text{Lab}} = 135^\circ$, $\theta_{\text{Lab}} = 90^\circ$, whereas the rest of the cylinders were randomly oriented along both φ_{Lab} and θ_{Lab} .

RESULTS

Figure 2a shows the $E(\psi)$ raw data images obtained from the d-PGSE MRI with EPI readout in the ex vivo rat brain. The raw data clearly demonstrate that signal intensity variation occurs in many parts of the brain when ψ is varied. In several cortical regions, for example, the image intensity clearly diminished between $\psi = 0^\circ$ and $\psi = 90^\circ$ (arrow). Then, the image intensity increased between $\psi = 90^\circ$ and $\psi = 180^\circ$, where the intensity appeared very similar to the intensity at $\psi = 0^\circ$. This $E(\psi)$ oscillation then appears to be mirrored up to $\psi = 360^\circ$.

Figure 2b shows the normalized data, i.e., the $E(\psi)_{\text{norm}}$ images. Note that when the images are normalized, T_2 - and q -value-induced contrasts are eliminated, and the intensity variation between the images now arises solely from the angular dependence. As a consequence of normalization, the $E(\psi = 0^\circ)_{\text{norm}}$ appears uniform and is close to unity in all pixels. In the normalized data, the relative oscillations appear much more clearly compared to the raw data and can be appreciated across the entire brain. In some cortical regions, the signal decreases by up to $\sim 50\%$ compared to its original $E(\psi = 0^\circ)$ value, whereas in organized regions such as the corpus callosum, the signal increases by up to $\sim 90\%$ from its original value. Such strong variations are evident in most brain regions and especially in gray matter.

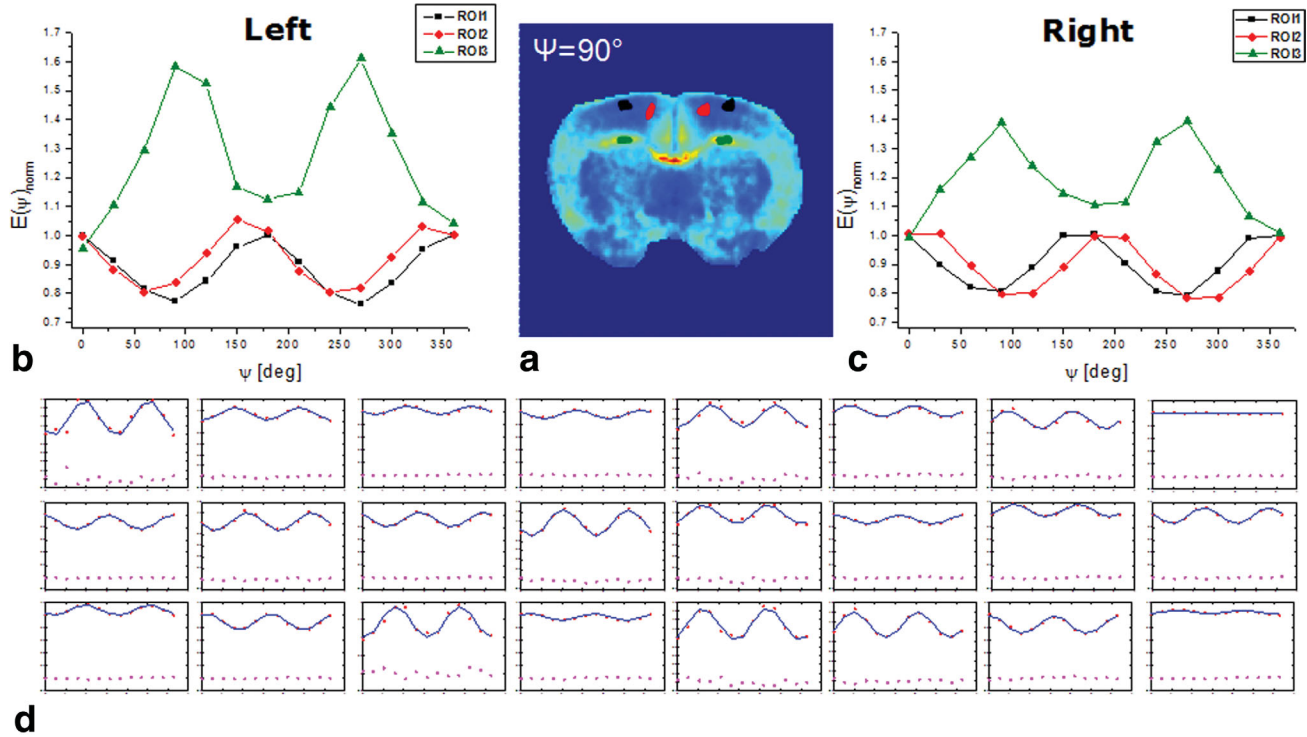


FIG. 3. **a:** ROIs shown on the $\psi = 90^\circ$ d-PGSE MRI images. **b:** The $E(\psi)_{\text{norm}}$ signal oscillations for the three ROIs shown in (a) on the left hemisphere. **c:** The $E(\psi)_{\text{norm}}$ signal oscillations for the three ROIs shown in (a) on the right hemisphere. Three distinct behaviors can be viewed, a nearly perfect oscillation (ROI 1), a phase-shifted oscillation (ROI 2), and an opposite oscillation (ROI 3). **d:** Twenty-four clusters of the pixels in the brain, showing the robust angular patterns in the $E(\psi)_{\text{norm}}$ (red asterisks), the fit to Eq. 1 (lines) and the errors (pink asterisks). Equation 1 describes all clusters adequately, and the errors are close to zero for all clusters. Note that this cluster analysis was only performed to show the robustness of the data, all datasets were eventually analyzed pixel-by-pixel, with no clustering. [Color figure can be viewed in the online issue, which is available at wileyonlinelibrary.com.]

Figure 3 shows a region of interest (ROI) analysis of six ROIs placed within the rat brain. Figure 3a shows an $E(\psi = 90^\circ)_{\text{norm}}$ image overlaid with three representative ROIs in each hemisphere. In the first ROI in the left hemisphere (black), a nearly perfectly symmetrical $E(\psi)_{\text{norm}}$ oscillation is observed (Fig. 3b, black symbols). However, in an adjacent ROI (red), while the amplitude of the oscillation appears quite similar to the first ROI, the symmetry about $\psi = 180^\circ$ is broken, and a phase shift of $\sim 30^\circ$ emerges (Fig. 3b, red symbols). In the WM of the left hemisphere (green ROI), the $E(\psi)$ dependence appears as a mirror image of the oscillations in the cortex. In the right hemisphere, similar trends were observed (Fig. 3c) with one noticeable difference: the phase shift in the red ROI appeared “opposite” compared to the phase shift in the left hemisphere (Fig. 3c, red symbols). After inspecting the pixels in many slices and brains using different parameters, we find that the vast majority of pixels display similar oscillation characteristics as described earlier. We found that nearly all of these oscillations can be robustly fitted to Eq. 1. To demonstrate the robustness of the analysis, we clustered the pixels to 24 clusters using a k -means clustering algorithm, which represent the signal oscillation in the entire brain. Figure 3d shows the experimental data (red) along with the fit to Eq. 1 (blue line) and the error of the fit (pink asterisks). It should be noted that the clustering was performed only for the purpose of this demonstra-

tion, whereas in all the following results below, a pixel-by-pixel analysis was performed. Note that in many clusters, a phase is clearly observed in the $E(\psi)_{\text{norm}}$ data, and that Eq. 1 fits nicely to all the data (Fig. 3d).

The origin of the phase shift can be quite easily attributed to residual ensemble anisotropy within mostly randomly oriented compartments by a qualitative inspection of the signal decay in the angular experiment (data not shown). However, a more quantitative approach for analyzing such a scenario can be employed using the analytical expressions presented in Ref. 26. Figure 4 shows the theoretical prediction for $E(\psi)$ in three different scenarios: cylinders that are completely randomly oriented (red) and cylinders that are residually coherently oriented in the X - Y plane, i.e., at $\theta_{\text{Lab}} = 90^\circ$ with $\phi_{\text{Lab}} = 45^\circ$ axis (green) or $\phi_{\text{Lab}} = 135^\circ$ axis (blue). When all compartments are randomly oriented, the signal oscillation is completely symmetrical, whereas a phase emerges only when residual ensemble anisotropy exists. Note that here, the phase does not exactly match the tilt angles, as only 30% of the compartments are characterized by ensemble anisotropy, whereas 70% of the compartments are completely randomly oriented. Nevertheless, the phase shift reveals the presence of residual ensemble anisotropy within the system.

After verifying that the data fit well to the phenomenological equation, the $E(\psi)_{\text{norm}}$ images of the rat brain were fit to Eq. 1 on a pixel-by-pixel basis. Figure 5a,b

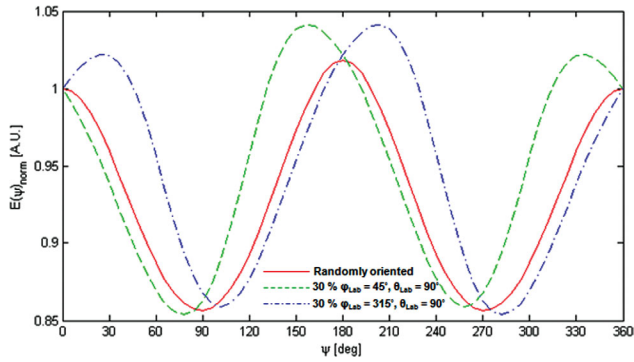


FIG. 4. Analytical curves of $E(\psi)_{norm}$, based on the theory in Ref. 26 describing different underlying microstructural scenarios: completely randomly oriented cylindrical compartments (red), 30% coherently organized compartments along $\theta_{Lab} = 90^\circ$ with $\phi_{Lab} = 45^\circ$ axis (green) or $\phi_{Lab} = 135^\circ$ axis (blue), whereas 70% are completely randomly oriented. Note the phase that emerges in the signal in case of some residual coherence. [Color figure can be viewed in the online issue, which is available at wileyonlinelibrary.com.]

shows maps based on apparent eccentricity, whereas Fig. 5c,d shows maps based on the residual phase, ϕ . Figure 5a shows that under the experimental conditions used here, the aE values vary between ~ -0.8 and 0.8 in the brain. The aE maps appear quite symmetrical when the two hemispheres are compared, and several remarkable features can be noted. First, when cortical gray matter is inspected from its superior part toward the inferior part of the cortex (i.e., from superior pial surface toward the WM of the corpus callosum), a contrast arises, showing between five and six “layers” in the aE maps. Furthermore, a distinct contrast emerges between the areas of the most medial part of the gray matter, which has negative aE (thus appearing blue), and the more lateral gray matter area, which has a positive aE. The gray matter of

the striatum also shows nonuniformity in aE contrast; furthermore, the striatal gray matter has different aEs compared with cortical gray matter (Fig. 5a). Note that in these aE images, the WM (e.g., the corpus callosum) does not appear homogeneous but shows a variation in the sign of aE along the WM: in the regions where the corpus callosum is more aligned in the medial–lateral direction, the aE appears negative, whereas where it is aligned in a more superior–inferior direction, the aE is positive. Figure 5b shows a map of absolute-valued aE, $|aE|$. Here, the WM of the corpus callosum appears more uniform; however, in the cortical gray matter, the layering is still clearly evident, and the contrast within the striatum remains robust. In some cases, the aE values for cortex and WM are similar in magnitude.

Figure 5c shows the map of the residual phase, ϕ . These images reveal strong contrast, especially in gray matter regions of the cortex. Looking from the most medial part laterally in the cortex, the ϕ parameter creates a contrast that appears as “bands” of varying ϕ -values across the cortex. Notably, the variation in the values of ϕ in one hemisphere is mirrored in the second hemisphere, but with opposite signs of ϕ ; this indeed reflects the opposite residual orientations due to ensemble anisotropy of compartments in the gray matter between the two hemispheres. To verify that the ϕ -values are indeed symmetrical across the brain, the colorbar was symmetrized with respect to 0; indeed, a highly symmetrical image of ϕ_{sym} is then obtained (Fig. 5d). Note also the strong contrast that appears in the gray matter of the striatum in both ϕ and ϕ_{sym} maps, where the contrasts are opposite in sign in ϕ and highly symmetrical in ϕ_{sym} .

To show that these phenomena are general and robust, we performed similar d-PGSE MRI experiments in several rat brains and in different brain slices, and with different imaging gradient orientations. The results are

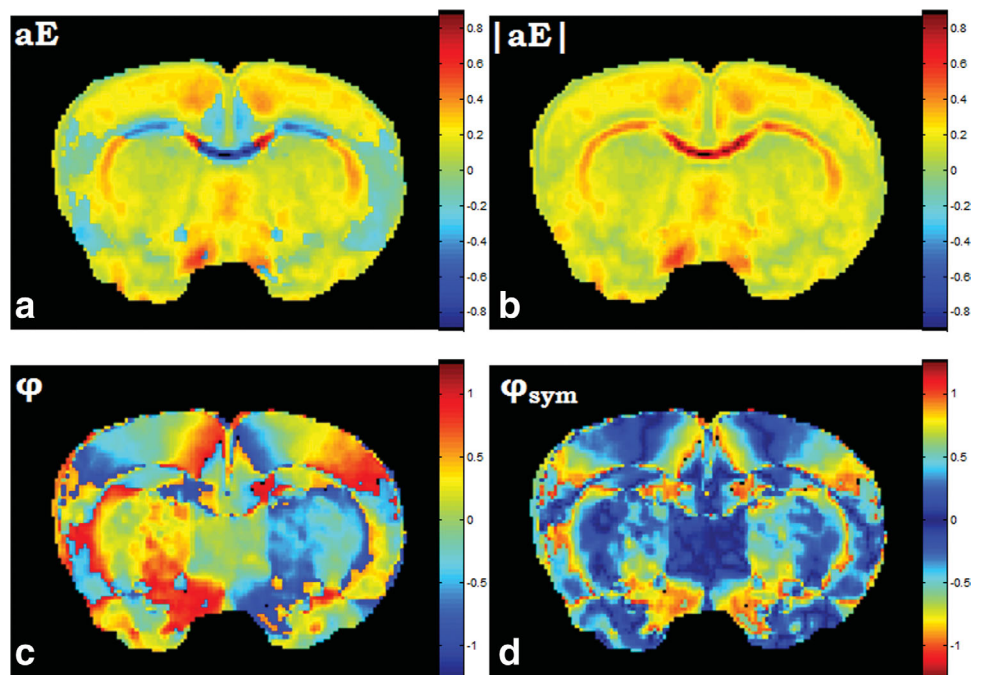


FIG. 5. **a:** Apparent eccentricity (aE) map. **b:** Absolute-valued apparent eccentricity map ($|aE|$). **c:** Map of the residual ensemble anisotropy phase ϕ . **d:** Maps of the symmetrized phase, ϕ_{sym} , where the negative colorbar was made equal to the positive colorbar. Note the marked contrast in cortical regions in these images, especially the contrast resembling cortical layering in the aE map and the strong contrast in the medial–lateral direction observed in the ϕ maps. The experiments were performed in the X–Y plane. [Color figure can be viewed in the online issue, which is available at wileyonlinelibrary.com.]

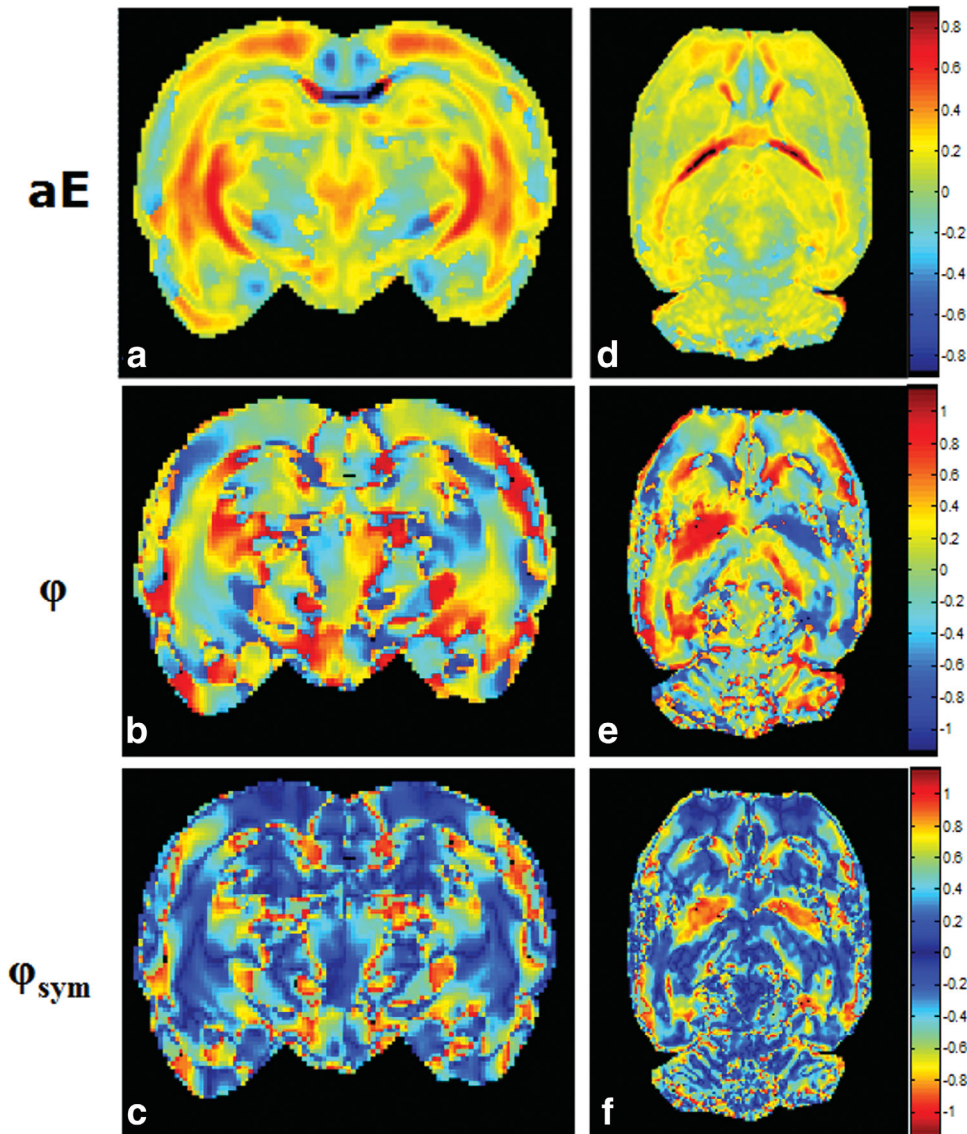


FIG. 6. **a–c**: Apparent eccentricity (aE), residual phase (ϕ), and symmetrized residual ensemble anisotropy phase (ϕ_{sym}) maps for a coronal slice from a different brain and from a more posterior position (compared to Fig. 5). **d–f**: Apparent eccentricity, ϕ and ϕ_{sym} maps for an axial slice from yet another different rat brain. These images show the robustness of the analysis across specimens and that imaging gradients do not contribute artifacts owing to cross-terms. Note the abundance of contrast especially in gray matter regions. The experiments were performed in the X–Y plane. [Color figure can be viewed in the online issue, which is available at wileyonlinelibrary.com.]

summarized in Fig. 6. Figure 6a–c shows the aE , ϕ , and ϕ_{sym} of a more posterior coronal slice (compared to Fig. 5) and Fig. 6d–f shows an axial slice from a different rat brain. All the trends that were outlined earlier appear robust across the different brains and regardless of the direction of the imaging gradients. Note the high medial-to-lateral symmetry in the aE and the ϕ_{sym} maps. In the more posterior slice, layers of the hippocampus are highly delineated in the aE maps (Fig. 6a–c).

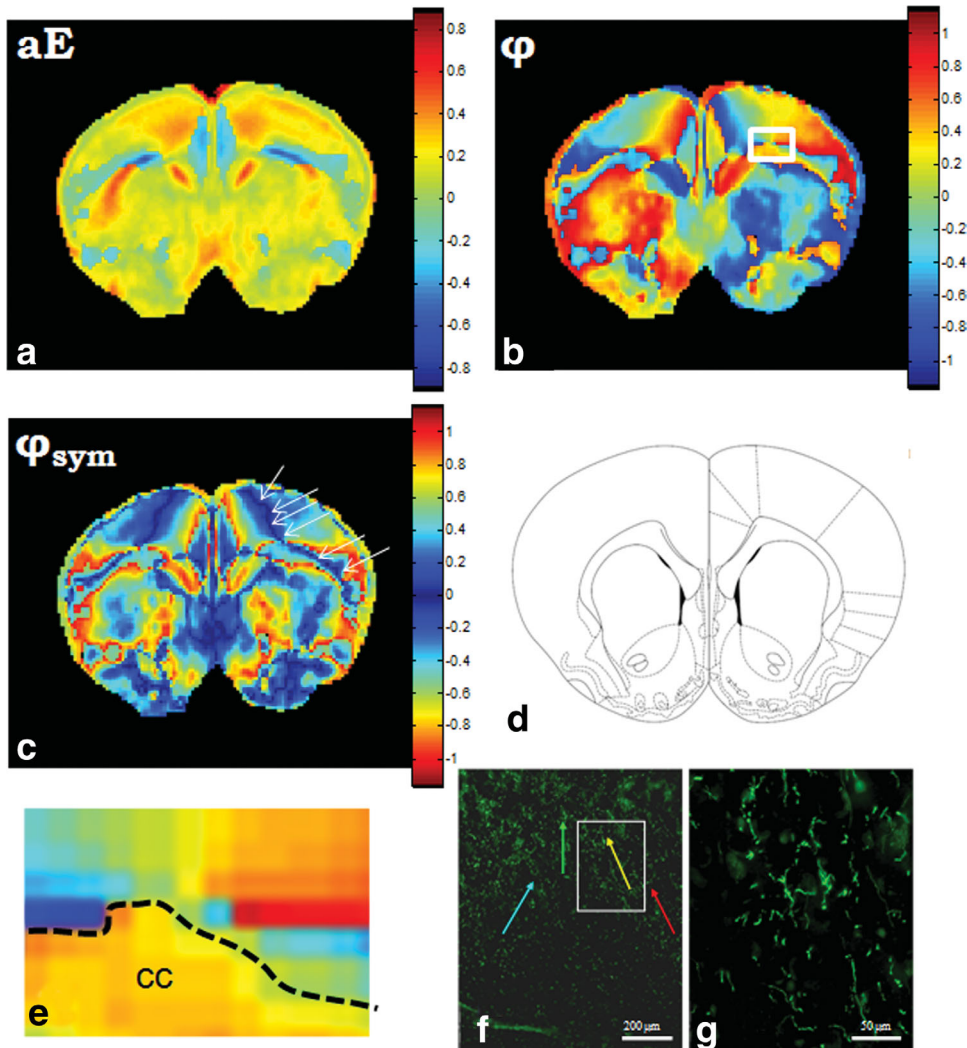
Figure 7 shows aE , ϕ , and ϕ_{sym} maps of yet another rat brain adjacent to the corresponding anatomical atlas slice (42). In the cortical gray matter, a strong contrast showing cortical layers is apparent (Fig. 7a). The ϕ and ϕ_{sym} maps show many different bands of ϕ in the gray matter (Fig. 7b,c). Some of these bands having the same value of ϕ even appear to run through different regions of the cortex (Fig. 7c, arrows), although it is premature to imply connectivity between different cortical regions based on the ϕ -value. The corresponding anatomical atlas (Fig. 7d) shows fewer regions within the cortical gray matter compared to the ϕ -contrast. However, it

should be noted that this could be due to the partial volume effect of more posterior parts of the brain in the MRI image, which cannot be viewed in the atlas, or due to a possible orientational dependence of the ϕ parameter.

Several interesting spatial patterns arise in these images. Note the contrast marked with arrows in Fig. 7c, which appears highly symmetrical in the contralateral hemisphere—this contrast is clearly not present in the anatomical atlas. Note that a similar spatial pattern to that delineated with the arrows in Fig. 7c can also be observed in Fig. 5d, in a completely different brain and in a more posterior slice.

Figure 7e shows an enlargement of the box highlighted in Fig. 7b. Note that in the cortex, a contrast arises from left to right in the form of ϕ -values varying from negative to positive values. Histological staining for TH⁺ neurons (Fig. 7f,g) shows a “diluted” view of the neuronal cytoplasm. Some residual ordering within the stained region can be observed, demonstrating that the orientation varies in its direction across the section. Inspecting the

FIG. 7. **a**: Apparent eccentricity map, **(b)** φ map and **(c)** φ_{sym} map of a coronal slice of the rat brain. **d**: The anatomical map (42) corresponding to the MRI image. **e**: Enlargement of the box in **(b)**. The end of the corpus callosum (cc) and the beginning of the cortex are delineated by the dashed line. **f**: Staining for TH⁺ neurons. **g**: Enlargement of the in **(f)**. Note that some residual ordering can be observed. [Color figure can be viewed in the online issue, which is available at wileyonlinelibrary.com.]



images with higher magnification reveals the slight ordering more clearly (Fig. 7g).

Although a direct comparison between d-PGSE MRI-derived indices and conventional DTI-derived indices is beyond the scope of this article, such a preliminary comparison is shown in Fig. 8 for ex vivo rat brain. Figure 8a,b shows the aE and φ maps, respectively, while the eigenvalues λ_i and their corresponding eigenvectors e_i obtained from DTI are shown in Fig. 8c,e, and g and Fig. 8d,e, and i, respectively. The aE map appears to show more contrast in the gray matter, especially in the cortex, compared to the individual eigenvalues. Interestingly, the φ map obtained from d-PGSE MRI and the primary eigenvector e_1 bear some resemblance. Notably, some bands of varying direction of e_1 can be detected in the cortex, although the φ maps do seem to show more fine details. The other eigenvectors seem to bear little resemblance with the φ parameter, as could perhaps be expected because they should point perpendicular to oriented fibers. However, it seems that further studies, both experimental and theoretical, will be needed to more directly compare the information available from DTI and the different parameters extracted from angular d-PGSE MR.

We then investigated the possibility of performing d-PGSE MRI experiments in the rat for the first time. Figure 9 shows in vivo d-PGSE MRI images obtained from a rat brain along with conventional DTI experiments. A contrast resembling cortical layering can be viewed in the gray matter in vivo from the aE maps (Fig. 9a) obtained from the d-PGSE MRI. The φ maps of the rat brain in vivo show the same trends as observed ex vivo (Fig. 9b). Note that many bands of varying values of φ can be observed in the cortex, showing remarkable contrast and providing contrast that is probably based on residual ensemble anisotropy of compartments within the gray matter region.

The FA maps derived from DTI experiments in vivo in the same brain showed, as expected, high fractional anisotropy in the WM regions, whereas in the gray matter, little contrast and low FA values were observed, although some layering is also evident in the FA derived from DTI images (Fig. 9c). A map of the primary diffusion tensor eigenvector (Fig. 9d) seems to show different contrast compared to the φ maps in d-PGSE MRI in the gray matter, showing less radial “bands”; however, the origins of these differences remain to be tested in future

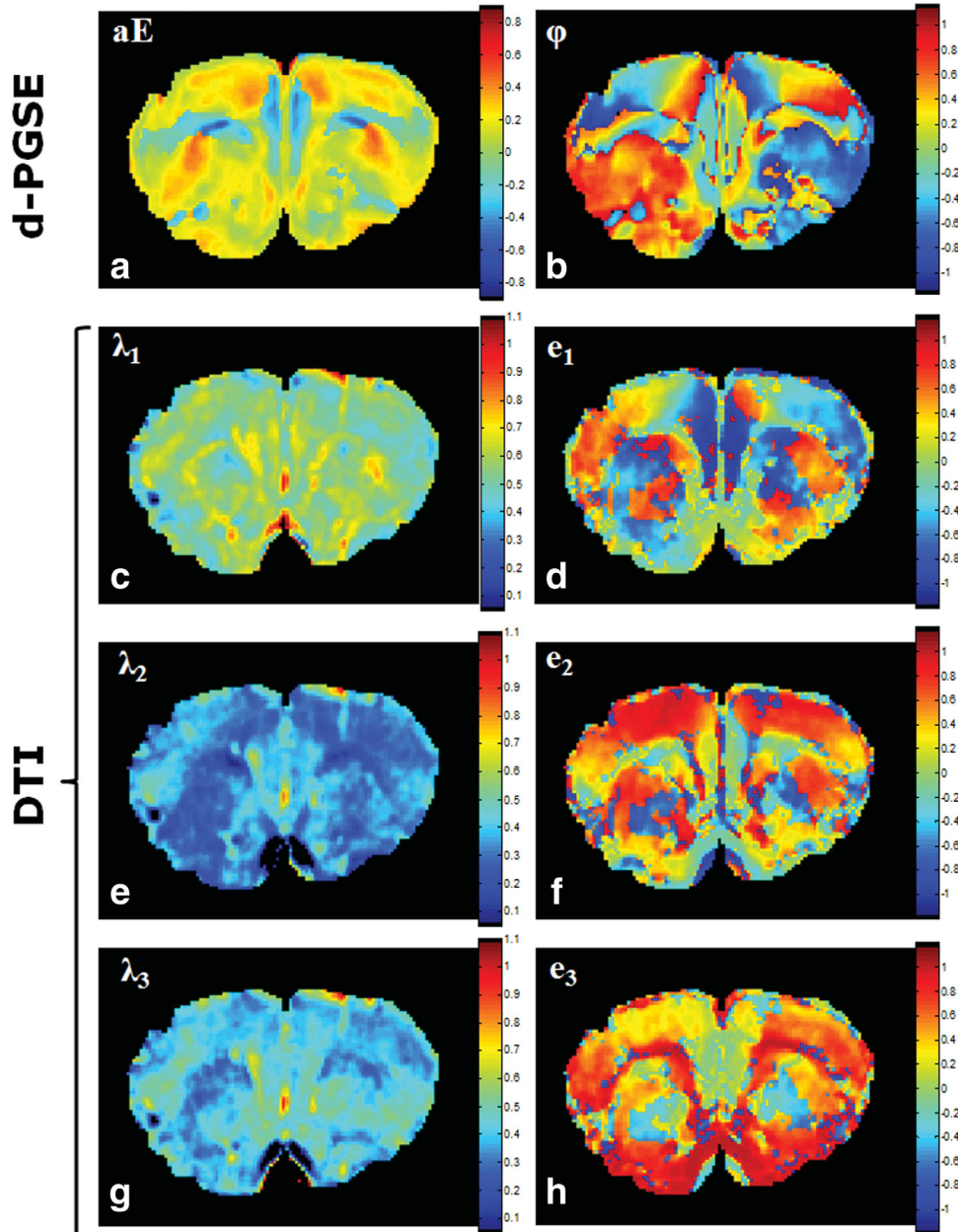


FIG. 8. **a,b**: d-PGSE MRI-derived maps. **b-h**: DTI-derived parameters. (a,b) represent aE and ϕ maps, respectively. c,e, and g: Maps of the eigenvalues λ_1 , λ_2 , and λ_3 and (d,f, and h) maps of eigenvectors e_1 , e_2 , and e_3 , respectively. The contrast observed in the ϕ maps resembles the contrast in the primary eigenvector, to a certain extent. However, further studies dedicated to comparison of d-PGSE MRI and DTI maps are required to establish the uniqueness of the contrasts observed. [Color figure can be viewed in the online issue, which is available at wileyonlinelibrary.com.]

studies dedicated to direct comparisons between the methods with different experimental parameters.

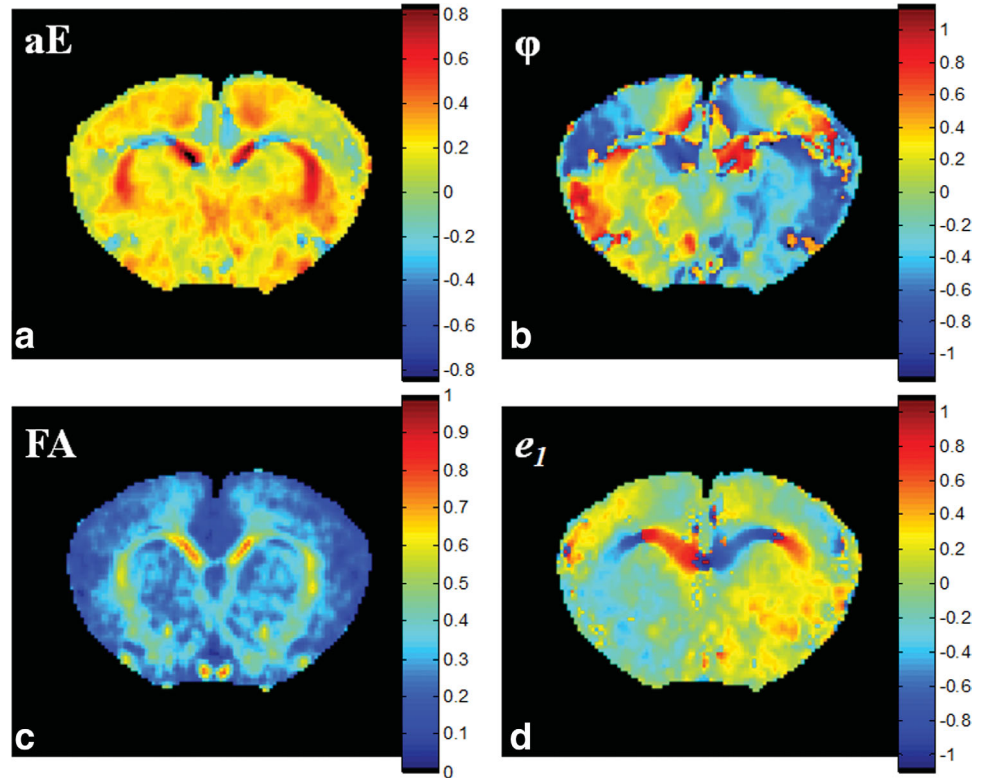
DISCUSSION

Single-PFG MR methods are capable of detecting eA in coherently organized compartments, which make them very useful for characterizing WM in the CNS. Angular d-PFG MR, which was first suggested theoretically by Mitra (19), can detect additional parameters such as microscopic anisotropy (μA) and compartment shape anisotropy (csA), and is therefore capable of providing novel microstructural information in more heterogeneous scenarios (30,31,41). Previous angular d-PFG MRI experimental studies involved sequences such as a multiple-spin echo sequence (20) that was performed on phantoms and spinal cord, a double-stimulated-echo MRI

sequence with EPI readout that was performed at 17.6 T and focused on the WM of the ex vivo rat spinal cord at short t_m (21), and a d-PFG-filtered MRI sequence that was performed on a glass capillary array phantom (43). Furthermore, angular d-PFG MRI was even performed very recently on a clinical scanner in phantoms and even spinal cords in the aim of detecting rotationally invariant indices for microstructure (39). In this study, we used a d-PGSE MRI sequence with EPI readout, that was performed at long t_m in the rat brain both ex vivo and in vivo, on a conventional 7-T scanner, and investigated the angular dependence and the information that can be obtained from it especially in gray matter tissues.

The gray matter is a highly heterogeneous tissue, comprised mostly of neuronal cell soma, axons, dendrites, as well as neuroglia and connective tissue. In the rodent, cortical layering of the gray matter is evident under

FIG. 9. **a**: Apparent eccentricity (aE) map of the brain in vivo. **b**: Residual ensemble anisotropy phase (ϕ) map of the same rat brain in vivo. (a,b) Derived from the analysis of the d-PGSE MRI results. **c**: FA map of the in vivo rat brain derived from DTI results. **d**: e_1 (primary eigenvector) map for the same rat in vivo. (c,d) Derived from the analysis of the DTI results. Note the strong contrasts that are observed in the cortex in vivo using d-PGSE MRI. [Color figure can be viewed in the online issue, which is available at wileyonlinelibrary.com.]



histology in the superior–inferior aspect of the brain (44), and different cytoarchitectonic features such as varying cell densities can be observed in the medial–lateral aspect (45). Extremely high-resolution MRI images show cortical layering even in T_2 -weighted images (46), and injection of contrast agents such as $MnCl_2$ also seems to generate contrast within the cortical layers of the rat neocortex (47).

Owing to the high microstructural heterogeneity of the gray matter, low FA values are generally detected in DTI studies of the rodent gray matter although in some cases, color-coded FA images do show some contrast in medial–lateral directions, as well as some degree of cortical layering (11,12). Although high FA values in WM correspond to the eA present, the low FA values in gray matter are more difficult to interpret. Therefore, methods such as angular d-PFG MRI that report on other microstructural parameters such as μA , which reflects compartment size and csA , which reflects the compartment eccentricity, may afford new sources of contrast in the gray matter. Previous studies using d-PGSE MR (17,18) showed qualitative differences between $E(q)$ plots at $\psi = 0^\circ$ and $\psi = 90^\circ$ in monkey gray matter (17); moreover, more recent studies showed that very accurate compartment sizes can be quantitatively extracted using this methodology in coherently organized (22) as well as randomly oriented pores (29). However, the gray matter tissue is highly complex, and each of the gray matter components (cell bodies, axons, etc.) may be characterized by its size distribution, its shape, as well as its volume fraction. Furthermore, each component may exhibit further compartmentation into, for example, intracellular and extracellular spaces, which may have their own

unique size and shape distributions. Another factor is exchange between these compartments and between the different components. A general model that accurately takes into account the fractional contribution of such microstructural elements and especially the size and shape distributions of intracellular and extracellular compartments is not yet available; therefore, we did not attempt to fit the d-PGSE MRI data to the elaborate theory that was so far published (25–27,32,33) or attempt to extract absolute information, such as axon size or eccentricity; indeed, such quantitative description would require numerous assumptions on the μA , csA , and eA of each of the microstructural elements that were mentioned earlier. Rather, we attempted to fit the data using a phenomenological equation that would fit to the vast majority of pixels in the brain, and indeed we found that Eq. 1 is adequate. Indeed, microstructural parameters such as the apparent eccentricity (aE) and the residual ensemble anisotropy (ϕ) could be quantified and mapped and were found to be consistent and robust across brains, slices, and imaging planes. Moreover, these parameters seem to provide additional sources of contrast for the rat brain, especially in the gray matter; an added value of these parameters is that they arise solely from restricted diffusion.

One of the major findings of this study is that signatures for csA were detected for the first time in the rat brain at long t_m , e.g., in regions where $\phi = 0^\circ$, the $\cos 2\psi$ profiles are a direct indication of randomly oriented anisotropic compartments. In other grey matter regions, we found that a phase emerges in the signal oscillation. This is the first study to report this feature of $E(\psi)$ in angular d-PFG MR; it seems that the phase originates from

residual ensemble anisotropy of coherently organized compartments in otherwise disordered media. The ϕ maps seem to reveal new source of contrast in the brain, showing very strong variance of compartments across the cortex. We decided to first follow TH⁺ neurons, which represent an important population of the GM neurons, and found some correlation to the ϕ maps; however, assigning the residually oriented compartments in the gray matter to a biological component is by no means straightforward. We chose TH⁺ neurons because we assumed that nonspecific evaluation would be difficult to correlate with the d-PFG MR findings. Indeed, even in WM, where compartments are coherently organized and fully myelinated, the relative importance of the different WM components to the diffusion anisotropy observed in DTI remains highly debated (48–50). It should be noted that in some cases, the low FA as well as the primary eigenvector obtained from DTI in GM were tentatively correlated with apical dendrites that are radially oriented within the gray matter (51,52), and that in other cases, connections could be identified between these regions (6). More histological studies are needed to directly infer on the source of aE and ϕ and their correlation with cytoarchitectonic features of the gray matter.

The experiments in this study were performed at the long t_m regime since there, μA effects are decoupled from the signal and allow a more clear view of csA effects. In this study, a mixing time of ~ 15 ms was chosen under the assumption that this duration is sufficient to reach the long t_m regime in CNS tissues. Indeed, in regions clearly characterized by randomly oriented compartments $E(\psi = 0^\circ) \sim E(\psi = 180^\circ)$ is expected for complete decoupling of μA from the signal. However, in highly heterogeneous systems, defining the long t_m regime is not straightforward owing to the distributions of sizes and shapes in the specimen. The $E(\psi)$ dependencies shown in this study revealed little signal differences between $E(\psi = 0^\circ)$ and $E(\psi = 180^\circ)$, as expected when μA is completely decoupled from the angular profile, thus showing that this time scale is sufficiently long to be described as long t_m . Fixation may affect the duration required to decouple μA from csA, but in this study, it seems that the mixing time was sufficiently long in both ex vivo and in vivo tissues. This is consistent with previous studies showing that the long t_m regime is reached easily in other systems (53).

Although the angular dependencies in this study were only acquired at a single q -value in the rat brain, we note that the aE maps are inherently dependent on the q -values used (data not shown). When angular d-PGSE MRI data will be analyzed with adequate theoretical models that should be developed in future studies, the different aE maps at different q -values will yield the same eccentricity (but not the same apparent eccentricity) for monodisperse compartments (in both size and shape). However, we note by passing that when heterogeneous systems (in size and/or in shape) are considered, the angular d-PGSE MRI may hold yet another advantage: at different q -values, different microstructural elements (i.e., different length scales or eccentricities) will be emphasized differently at each q -value (similarly to the “shutter-speed” effect (54)); therefore, analysis of

angular profiles at different q -values may well portray different microstructural elements, manifesting different eccentricities at different q -values. This indeed is a manifestation of the added dimension of ψ at each q -value, as compared with, for example, q -space MR, which averages out the information from the concurrent analysis of many individual q -values.

Although the potential of d-PGSE MRI to uncover underlying microarchitectural features in the brain in vivo seems promising, there also exist some limitations. First, angular d-PGSE MRI is not invariant to rotation in cases where residual ensemble anisotropy exists, and therefore, the aE and ϕ maps are very strongly dependent on the plane of acquisition, i.e., the plane where the angle ψ is varied. Therefore, if the brain is tilted or if the plane of acquisition is tilted with respect to the brain, the aE and ϕ results may vary strongly. Compared to the rotationally invariant DTI parameters, this is an apparent drawback of the proposed analysis scheme. Nevertheless, in this study, care was taken to align the brains in the magnet, and the aE and ϕ results were repeatedly reproducible. Another limitation that arises from this rotational dependence is that the ϕ maps need to be inspected with close correlation to the aE maps, as ϕ can have the same value when $aE < 0$ or $aE > 0$. Further studies are needed to develop methods that will efficiently measure indices that are invariant to rotations and compare them to what is obtained from different planes of acquisition in d-PGSE MRI. Indeed preliminary theoretical studies attempting to solve this problem are already emerging (32,33). Meanwhile, the experiment can be conducted in the X–Y plane simply by either ensuring that the brains are perfectly aligned or by carefully rotating the plane of acquisition with the tilt angle of the brain.

Another limitation is that the gradients used in this study were stronger (~ 360 mT/m) than those found in the clinical scanners (up to 80 mT/m). To achieve the same q -value used in this study using the maximum clinically available gradients, one would need to prolong the diffusion gradient duration by a factor of ~ 4.5 . Although it was predicted that prolonging the diffusion gradient duration would reduce the amplitude of the oscillations (26,28), it remains to be seen how d-PGSE MRI performs in vivo on clinical MRI scanners; a recent study suggested that d-PGSE MRI could indeed be feasible in a clinical scanner using ex vivo pig neuronal tissues (39).

In several recent spectroscopy studies (29–31), angular d-PFG MR was performed using bipolar gradients to overcome susceptibility-induced background gradients that may affect the angular profile (55). The calibration d-PGSE MRI experiments show that these effects are not very significant here (data not shown); however, we cannot completely exclude that cross-terms between background gradients (or even imaging gradients) contribute, to a certain extent, to some of the angular profiles shown here.

Finally, we have shown a preliminary comparison of angular d-PGSE MRI to DTI scans in the ex vivo and in vivo brains. Although it seems that angular d-PGSE MRI shows novel contrasts, especially in the GM, we note that a direct comparison was beyond the scope of this

article, and that it could be expected that the contrasts are dependent on experimental parameters such as q -values, Δs , as well as others. The primary eigenvector in DTI should point to the direction of residually oriented compartments, and the differences between ϕ and e_1 may be due to variations in experimental parameters, at least to a certain extent. To infer on the utility and the added value of d-PGSE MRI and the contrasts that can be obtained from it, further future studies dedicated to more directly compare between the two methods at various experimental parameters are needed, as well as comparisons between d-PGSE MRI with other methods such as q -space imaging or other more advanced diffusion MRI methods.

CONCLUSIONS

In conclusion, d-PGSE MRI was performed at long t_m in the rat brain both *ex vivo* and *in vivo* for the first time. We presented a simple and robust analysis method for the data, which result in quantifiable maps of apparent eccentricity (aE) and residual phase (ϕ). These maps showed interesting contrasts, especially within gray matter structures, that are relatively difficult to characterize using conventional s-PFG MR methods. This promising approach may become important in studying normal, developmental and neuropathological processes in the CNS and especially in the gray matter in both basic and applied sciences.

ACKNOWLEDGMENTS

N.S., D.B., Y.A., L.B., and Y.C. were partially supported by the CONNECT consortium administered by the European Commission under framework package 7. The MRI scanner used in this study was purchased with grants from the Israel Science Foundation and The Raymond and Beverly Sackler Center for Biophysics, Tel Aviv University, and is operated by the Alfredo Federico Strauss Center for Computational Neuro-Imaging, Tel Aviv University. N.S. thanks the Clore Scholars Program for a scholarship.

REFERENCES

- Varela F, Lachaux JP, Rodriguez E, Martinerie J. The brainweb: phase synchronization and large-scale integration. *Nat Rev Neurosci* 2001;2:229–239.
- Moseley ME, Cohen Y, Mintorovitch J, Chileuitt L, Shimizu H, Kucharczyk J, Wendland MF, Weinstein PR. Early detection of regional cerebral-ischemia in cats—comparison of diffusion-weighted and T_2 -weighted MRI and spectroscopy. *Magn Reson Med* 1990;14:330–346.
- Moseley ME, Cohen Y, Kucharczyk J, Mintorovitch J, Asgari HS, Wendland MF, Tsuruda J, Norman D. Diffusion weighted MR imaging of anisotropic water diffusion in cat central-nervous-system. *Radiology* 1990;176:439–445.
- Basser PJ, Mattiello J, Lebihan D. Diffusion tensor spectroscopy and imaging. *Biophys J* 1994;66:259–267.
- Izhikevich EM, Edelman GM. Large-scale model of mammalian thalamocortical systems. *Proc Natl Acad Sci USA* 2008;105:3593–3598.
- Behrens TEJ, Johansen-Berg H, Woolrich MW, Smith SM, Wheeler-Kingshott CAM, Boulby PA, Barker GJ, Sillery EL, Sheehan K, Ciccarelli O, Thompson AJ, Brady JM, Matthews PM. Non-invasive mapping of connections between human thalamus and cortex using diffusion imaging. *Nat Neurosci* 2003;6:750–757.
- Hagmann P, Sporns O, Madan N, Cammoun L, Pienaar R, Wedeen VJ, Meuli R, Thiran JP, Grant PE. White matter maturation reshapes structural connectivity in the late developing human brain. *Proc Natl Acad Sci USA* 2010;107:19067–19072.
- Horsfield MA, Jones DK. Applications of diffusion-weighted and diffusion tensor MRI to white matter diseases—a review. *NMR Biomed* 2002;15:570–577.
- Le Bihan D. Looking into the functional architecture of the brain with diffusion MRI. *Nat Rev Neurosci* 2003;4:469–480.
- Le Bihan D, Urayama S, Aso T, Hanakawa T, Fukuyama H. Direct and fast detection of neuronal activation in the human brain with diffusion MRI. *Proc Natl Acad Sci USA* 2006;103:8263–8268.
- Huang H, Yamamoto A, Hossain MA, Younes L, Mori S. Quantitative cortical mapping of fractional anisotropy in developing rat brains. *J Neurosci* 2008;28:1427–1433.
- Hui ES, Cheung MM, Qi LQ, Wu EX. Towards better MR characterization of neural tissues using directional diffusion kurtosis analysis. *Neuroimage* 2008;42:122–134.
- Kroenke CD, Van Essen DC, Inder TE, Rees S, Bretthorst GL, Neil JJ. Microstructural changes of the baboon cerebral cortex during gestational development reflected in magnetic resonance imaging diffusion anisotropy. *J Neurosci* 2007;27:12506–12515.
- Cory DG, Garroway AN, Miller JB. Applications of spin transport as a probe of local geometry. *Polymer Prepr* 1990;31:149–150.
- Cheng Y, Cory DG. Multiple scattering by NMR. *J Am Chem Soc* 1999;121:7935–7936.
- Callaghan PT, Komlosh ME. Locally anisotropic motion in a macroscopically isotropic system: displacement correlations measured using double pulsed gradient spin-echo NMR. *Magn Reson Chem* 2002;40:S15–S19.
- Komlosh ME, Horkay F, Freidlin RZ, Nevo U, Assaf Y, Basser PJ. Detection of microscopic anisotropy in gray matter and in a novel tissue phantom using double pulsed gradient spin echo MR. *J Magn Reson* 2007;189:38–45.
- Komlosh ME, Lizak MJ, Horkay F, Freidlin RZ, Basser PJ. Observation of microscopic diffusion anisotropy in the spinal cord using double-pulsed gradient spin echo MRI. *Magn Reson Med* 2008;59:803–809.
- Mitra PP. Multiple wave-vector extensions of the NMR pulsed-field-gradient spin-echo diffusion measurement. *Phys Rev B* 1995;51:15074–15078.
- Koch MA, Finsterbusch J. Compartment size estimation with double wave vector diffusion-weighted Imaging. *Magn Reson Med* 2008;60:90–101.
- Weber T, Ziener CH, Kampf T, Herold V, Bauer WR, Jakob PM. Measurement of apparent cell radii using a multiple wave vector diffusion experiment. *Magn Reson Med* 2009;61:1001–1006.
- Shemesh N, Özarslan E, Basser PJ, Cohen Y. Measuring small compartmental dimensions with low- q angular double-PGSE NMR: the effect of experimental parameters on signal decay. *J Magn Reson* 2009;198:15–23.
- Shemesh N, Özarslan E, Bar-Shir A, Basser PJ, Cohen Y. Observation of restricted diffusion in the presence of a free diffusion compartment: single- and double-PFG experiments. *J Magn Reson* 2009;200:214–225.
- Shemesh N, Özarslan E, Basser PJ, Cohen Y. Detecting diffusion-diffraction patterns in size distribution phantoms using double-pulsed field gradient (d-PFG) NMR: theory and experiments. *J Chem Phys* 2010;132:034703 (1-12).
- Özarslan E, Basser PJ. Microscopic anisotropy revealed by NMR double pulsed field gradient experiments with arbitrary timing parameters. *J Chem Phys* 2008;128:154511 (1-11).
- Özarslan E. Compartment shape anisotropy (CSA) revealed by double pulsed field gradient MR. *J Magn Reson* 2009;199:56–67.
- Özarslan E, Shemesh N, Basser PJ. A general framework to quantify the effect of restricted diffusion on the NMR signal with applications to double pulsed field gradient NMR experiments. *J Chem Phys* 2009;130:104702 (1-9).
- Koch MA, Finsterbusch J. Numerical simulation of double-wave vector experiments investigating diffusion in randomly oriented ellipsoidal pores. *Magn Reson Med* 2009;62:247–254.
- Shemesh N, Özarslan E, Adiri T, Basser PJ, Cohen Y. Noninvasive bipolar double-pulsed-field-gradient NMR reveals signatures for pore size and shape in randomly oriented, polydisperse, inhomogeneous porous media. *J Chem Phys* 2010;133:044705 (1-9).

30. Shemesh N, Adiri T, Cohen Y. Probing microscopic architecture of opaque heterogeneous systems using double-pulsed-field-gradient NMR. *J Am Chem Soc* 2011;133:6028–6035.
31. Shemesh N, Cohen Y. Microscopic and compartment shape anisotropies in gray and white matter revealed by angular bipolar double-PFG MR. *Magn Reson Med* 2011;65:1216–1227.
32. Finsterbusch J, Koch MA. A tensor approach to double wave vector diffusion-weighting experiments on restricted diffusion. *J Magn Reson* 2008;195:23–32.
33. Lawrenz M, Koch MA, Finsterbusch J. A tensor model and measures of microscopic anisotropy for double-wave-vector diffusion-weighting experiments with long mixing times. *J Magn Reson* 2009;202:43–56.
34. Jespersen SN, Buhl N. The displacement correlation tensor: microstructure, ensemble anisotropy and curving fibers. *J Magn Reson* 2011;208:34–43.
35. Finsterbusch J. Extension of the double-wave-vector diffusion-weighting experiment to multiple concatenations. *J Magn Reson* 2009;198:174–182.
36. Finsterbusch J. Numerical simulations of short-mixing-time double-wave-vector diffusion-weighting experiments with multiple concatenations on whole-body MR systems. *J Magn Reson* 2010;207:274–282.
37. Finsterbusch J. The parallel-antiparallel signal difference in double-wave-vector diffusion-weighted MR at short mixing times: a phase evolution perspective. *J Magn Reson* 2011;208:114–121.
38. Drobnjak I, Zhang H, Hall MG, Alexander DC. The matrix formalism for generalised gradients with time-varying orientation in diffusion NMR. *J Magn Reson* 2011;210:151–157.
39. Lawrenz M, Finsterbusch J. Detection of microscopic diffusion anisotropy on a whole-body MR system with double wave vector imaging. *Magn Reson Med* 2011;66:1405–1415.
40. Shemesh N, Özarslan E, Komlosh ME, Bassar PJ, Cohen Y. From single-pulsed field gradient to double-pulsed field gradient MR: glean new microstructural information and developing new forms of contrast in MRI. *NMR Biomed* 2010;23:757–780.
41. Finsterbusch J. Multiple-wave-vector diffusion weighted NMR. *Ann Rep NMR Spectrosc*. 2011;72:225–299.
42. Paxinos G, Watson C. *The rat brain*, 4th ed. San Diego: Academic Press; 1998.
43. Komlosh ME, Özarslan E, Lizak MJ, Horkay F, Schram V, Shemesh N, Cohen Y, Bassar PJ. Pore diameter mapping using double pulsed-field gradient MRI and its validation using a novel glass capillary array phantom. *J Magn Reson* 2011;208:128–135.
44. Polleux F, Dehay C, Kennedy H. The timetable of laminar neurogenesis contributes to the specification of cortical areas in mouse isocortex. *J Comp Neurol* 1997;385:95–116.
45. Caviness VS Jr. Architectonic map of neocortex of the normal mouse. *J Comp Neurol* 1975;164:247–263.
46. Boretius S, Kasper L, Tammer R, Michaelis T, Frahm J. MRI of cellular layers in mouse brain in vivo. *Neuroimage* 2009;47:1252–1260.
47. Aoki I, Wu YJL, Silva AC, Lynch RM, Koretsky AP. In vivo detection of neuroarchitecture in the rodent brain using manganese-enhanced MRI. *Neuroimage* 2004;22:1046–1059.
48. Beaulieu C. The basis of anisotropic water diffusion in the nervous system—a technical review. *NMR Biomed* 2002;15:435–455.
49. Lee JH, Springer CS. Effects of equilibrium exchange on diffusion-weighted NMR signals: the diffusigraphic “shutter-speed”. *Magn Reson Med* 2003;49:450–458.
50. Budde MD, Frank JA. Neurite beading is sufficient to decrease the apparent diffusion coefficient after ischemic stroke. *Proc Natl Acad Sci USA* 2010;107:14472–14477.
51. Kroenke CD, Bretthorst GL, Inder TE, Neil JJ. Diffusion MR imaging characteristics of the developing primate brain. *Neuroimage* 2005;25:1205–1213.
52. Mori S, Itoh R, Zhang JY, Kaufmann WE, van Zijl PCM, Solaiyappan M, Yarowsky P. Diffusion tensor imaging of the developing mouse brain. *Magn Reson Med* 2001;46:18–23.
53. Shemesh N, Özarslan E, Bassar PJ, Cohen Y. Accurate noninvasive measurement of cell size and compartment shape anisotropy in yeast cells using double-pulsed-field-gradient MR. *NMR Biomed*, in press; DOI 10.1002/nbm.1737.
54. Huang W, Li X, Morris EA, Tudorica LA, Seshan VE, Rooney WD, Tagge I, Wang Y, Xu JG, Springer CS. The magnetic resonance shutter speed discriminates vascular properties of malignant and benign breast tumors in vivo. *Proc Natl Acad Sci USA* 2008;105:17943–17948.
55. Shemesh N, Cohen Y. Overcoming apparent susceptibility induced anisotropy (aSIA) by bipolar double-pulsed-field-gradient NMR. *J Magn Reson* 2011;211:362–369.